Transactions of the Korean Nuclear Society Spring Meeting
Jeju, Korea, May 7–8, 2026

Extension of NuBDeC to Mirror Configuration

Tongnyeol Rhee[a*], Jisung Kang[b], Dami Jeong[c], Choongki Sung[c]
[a]KFE, Daejeon, Republic of Korea
[b]Tokamak Energy, Oxfordshire, United Kingdon
[c]KAIST, Daejeon, Republic of Korea

*Corresponding author: *trhee@kfe.re.kr

**Keywords : Nuclear Fusion, Mangetic Mirror, Neutral Beam Injection*

1. Introduction

Magnetic mirror systems have re-emerged as promising configurations for beam-driven fusion neutron sources due to their linear geometry, axial accessibility, and compatibility with high-power neutral beam injection (NBI) [1, 2]. In such systems, fusion reactivity is expected to be dominated by energetic beam ions rather than by the thermal background plasma, leading to strongly anisotropic and non-Maxwellian velocity distributions.

Accurate predictive modeling of beam-driven mirror plasmas therefore requires: (i) consistent magnetic field reconstruction in axisymmetric mirror geometry, (ii) flexible neutral beam geometry parameterization, (iii) evaluation of beam–beam fusion reactions using arbitrary distribution functions, and (iv) efficient treatment of long-time collisional relaxation in the presence of fast bounce motion. While these elements are individually well studied in tokamak contexts, their combined implementation in a magnetic mirror configuration has not been systematically addressed.

The Neutral Beam Deposition Code (NuBDeC) was originally developed for tokamak plasmas to compute beam ionization, slowing-down, and thermalization processes [3]. In the present work, NuBDeC is extended to operate in magnetic mirror geometry with three major developments.

First, a mirror-compatible beam injection model is implemented, allowing explicit specification of inlet position, aiming direction, aperture distribution, and angular divergence in cylindrical coordinates. This formulation enables realistic modeling of beam trajectories in linear devices without reliance on toroidal symmetry assumptions.

Second, a distribution-based beam–beam fusion reaction module is developed. Unlike conventional Maxwellian-based reactivity models, the present approach directly evaluates the reaction rate from the simulated (E, ξ) distribution function with gyro-phase averaging, using the Bosch–Hale cross-section formulation [4]. This enables consistent treatment of strongly anisotropic fast-ion populations in beam-driven mirror plasmas.

Third, the collisional acceleration scheme known as *Goosing* [5] is reformulated for magnetic mirror geometry. An event-driven implementation based on midplane crossing is introduced to separate bounce motion from slow collisional relaxation, allowing efficient long-time simulations while preserving orbit fidelity. To our knowledge, this is the first formulation of Goosing specifically adapted to linear mirror configurations.

To illustrate the capability of the extended framework, a counter-injected deuterium–tritium beam configuration is analyzed. This demonstration serves only to verify that the implemented modules operate self-consistently in a beam-driven mirror plasma. The primary objective of this paper is therefore not device performance prediction, but the presentation and validation of a unified computational framework for beam geometry, beam–beam fusion evaluation, and collisional acceleration in magnetic mirror systems.

The remainder of this paper is organized as follows. Section 2 describes the magnetic mirror geometry and the reconstruction of the axisymmetric magnetic field using GEQDSK-based poloidal flux representation. Section 3 presents the neutral beam geometry parameterization implemented for linear mirror devices. Section 4 details the distribution-based beam–beam fusion reaction model, including the gyro-phase averaging procedure and numerical benchmarking. Section 5 introduces the event-driven formulation of the Goosing scheme adapted to mirror bounce dynamics. Section 6 provides a demonstration case to verify the self-consistent operation of the implemented modules. Finally, Section 7 summarizes the main results and outlines future developments.

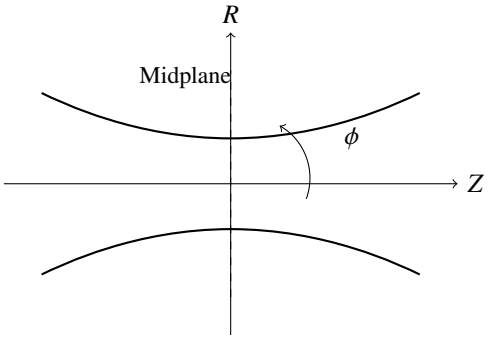

Figure 1: Schematic of the mirror geometry and coordinate system.

2. Mirror Geometry and Coordinate System

Before describing the beam injection model, we first define the magnetic geometry and coordinate system used in the mirror configuration.

The mirror device is modeled using a cylindrical coordinate system (R, ϕ, Z):

- R denotes the radial direction pointing toward the wall.
- ϕ is the azimuthal (toroidal) angle around the symmetry axis.
- Z denotes the axial direction aligned with the magnetic field.

The origin $(R, Z) = (0, 0)$ is defined at the midplane of the mirror device.

The magnetic field strength $B(Z)$ varies along the axial direction, reaching a minimum at the midplane and increasing toward the mirror throats. The mirror ratio is defined as

$$R_m = \frac{B_{\max}}{B_{\min}}. \tag{1}$$

Particles are confined if their pitch angle satisfies the mirror condition determined by R_m. Figure 1 illustrates the adopted coordinate system and magnetic configuration.

The magnetic geometry is imported using the standard tokamak equilibrium file format (GEQDSK), where the poloidal flux function $\psi(R, Z)$ is provided on a rectangular (R, Z) grid. Although GEQDSK is widely used for axisymmetric tokamak equilibria, the same representation can be employed to describe axisymmetric mirror fields by prescribing an appropriate $\psi(R, Z)$ map.

In the present implementation, the magnetic field is constructed from the poloidal flux as

$$\vec{B} = \nabla\psi \times \nabla\phi, \tag{2}$$

where ϕ is the azimuthal coordinate of the cylindrical system. This representation satisfies the solenoidal condition $\nabla \cdot \vec{B} = 0$ identically by construction, thereby ensuring divergence-free magnetic field reconstruction at the numerical level. The poloidal flux function $\psi(R, Z)$ is interpolated using a bicubic spline to obtain smooth first and second spatial derivatives. This is essential for continuously solving drift equations that require second derivatives of the magnetic field (or equivalently, of ψ) without introducing numerical discontinuities.

Using the spline-interpolated $\psi(R, Z)$, we reconstruct the magnetic field at arbitrary particle positions, and field-line trajectories are obtained by integrating along $\vec{B}$. In addition, guiding-center particle orbits are computed by solving the drift equations, which require continuous first and second derivatives of the magnetic field. The bicubic spline interpolation ensures sufficient smoothness for stable and accurate orbit integration.

Figure 2 shows the reconstructed poloidal flux, magnetic field lines, and representative 20 keV guiding-center particle orbits in the WHAM mirror configuration.[6] Two initial pitch-angle conditions are shown: one with $v_\parallel/v = \sqrt{0.5}$ (black solid line), and another with $v_\parallel/v = \sqrt{0.2}$ (blue dashed line). The resulting confined orbits demonstrate correct mirror reflection behavior and consistent drift motion along the field structure.

The agreement between field-line tracing and particle orbit evolution confirms that both the magnetic field reconstruction and the drift-equation implementation are correctly and consistently realized in the extended NuBDeC framework.

3. Neutral Beam Geometry Parameterization

The neutral beam (NB) injection geometry in the mirror configuration is implemented by a compact parameterization that specifies (i) the inlet location and aperture, (ii) the beam aiming direction in the (R, Z) plane, and (iii) the divergence model. Figure 3 illustrates the definition.

The inlet center of the i-th beamline is given in cylindrical coordinates by $(R_{\rm in}, \phi_{\rm in}, Z_{\rm in})$. The beam centerline is defined as the straight line from the inlet center to the impact point $(R_{\rm imp}, Z_{\rm imp})$ specified in the (R, Z) plane (see Fig. 3).

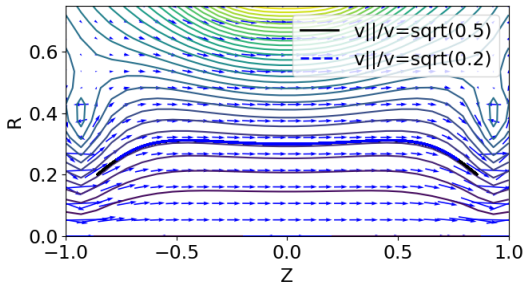

Figure 2: Spline-interpolated poloidal flux $\psi(R, Z)$ and magnetic field lines in the WHAM mirror configuration. Overlaid are 20 keV guiding-center particle orbits with $v_\parallel/v = \sqrt{0.5}$ (black solid line) and $v_\parallel/v = \sqrt{0.2}$ (blue dashed line). The results demonstrate proper magnetic field reconstruction and drift-orbit integration.

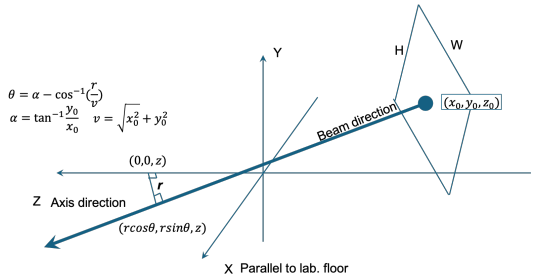

Figure 3: Schematic definition of the NBI geometry. The beam is defined by an inlet center position $(R_{\rm in}, \phi_{\rm in}, Z_{\rm in})$ and an aiming (impact) point $(R_{\rm imp}, Z_{\rm imp})$ in the poloidal plane. The inlet aperture is a rectangle with width/height, and particles are sampled with Gaussian weighting in the inlet coordinates and Gaussian angular divergence around the centerline.

The flag `side` (left/right) selects the injection side with respect to the device symmetry and fixes the corresponding beamline orientation. An example input block is:

```
beam.1.inlet_R   = 1.7
beam.1.inlet_phi = 0.0
beam.1.inlet_Z   = 1.9
beam.1.impact_R  = 0.01
beam.1.impact_Z  = -0.00
beam.1.side      = left

beam.1.width     = 0.1
beam.1.height    = 0.1
beam.1.sigma_u   = 0.05
beam.1.sigma_v   = 0.05
beam.1.sigma_div = 0.01
```

The inlet aperture is modeled as a rectangle with width `width` and height `height`. Particle launch points are sampled on this aperture using local inlet coordinates (u, v), where u and v denote the horizontal and vertical directions on the inlet plane, respectively. A Gaussian weighting is applied:

$$P(u, v) \propto \exp\left(-\frac{u^2}{2\sigma_u^2}\right) \exp\left(-\frac{v^2}{2\sigma_v^2}\right), \tag{3}$$

where σ_u and σ_v correspond to `sigma_u` and `sigma_v`. This enables realistic sampling of the injected neutral distribution across the injector footprint.

Beam divergence is included by applying a Gaussian angular spread about the centerline direction. The divergence standard deviation `sigma_div` sets the typical angular deviation of individual rays, thereby controlling the effective

beam emittance and spot broadening inside the plasma volume.

The ionization, charge-exchange, and slowing-down processes of injected neutrals are treated using the original NuBDeC without modification[3]. In particular, the beam ionization rate is computed using the same cross-section models and background plasma interaction framework previously validated for tokamak applications.

Thus, while the geometric definition of the beam has been reformulated for the mirror configuration, the underlying neutral ionization physics remains identical to the original NuBDeC implementation. This ensures consistency in beam deposition modeling and allows direct comparison between tokamak and mirror simulations within a unified framework.

4. Fusion Reaction Rate

In a magnetic mirror configuration, the thermal ion temperature is generally not high enough to produce a significant fusion reaction rate. Therefore, fusion reactions are primarily driven by energetic ions supplied by NBI. To accurately evaluate this contribution, a beam–beam fusion reaction rate module has been newly implemented.

The general fusion reaction rate is given by

$$R = \int f_1(\mathbf{v}_1) f_2(\mathbf{v}_2) \sigma(v_{\rm rel})\, v_{\rm rel}\, d^3v_1\, d^3v_2, \qquad (4)$$

where f_1 and f_2 are the velocity distribution functions, $v_{\rm rel} = |\mathbf{v}_1 - \mathbf{v}_2|$ is the relative velocity, and σ is the fusion cross section.

The reaction rate is evaluated using the beam distribution function obtained from simulation. A distribution diagnostic is constructed over a given time interval in the phase-space coordinates (R, Z, E, ξ), where E is the ion energy and $\xi = v_\parallel/v$ is the pitch variable. Here, $f(R, Z, E, \xi)$ denotes the particle density in energy–pitch space, such that integration over (E, ξ) yields the local beam ion density.

Assuming axisymmetry in velocity space, the 3D velocity-space integral can be expressed in (E, ξ, ϕ) coordinates, where ϕ is the gyro-phase angle. The ion speed is given by

$$v = \sqrt{\frac{2E}{m}}, \qquad (5)$$

with ion mass m.

For each spatial grid point (R, Z), the local fusion reaction rate is computed as

$$R = \iint dE_1\, d\xi_1\, dE_2\, d\xi_2\; f(E_1, \xi_1)\, f(E_2, \xi_2)\, \overline{\sigma v}_{12}. \qquad (6)$$

where $\overline{\sigma v}_{12}$ is the gyro-phase averaged fusion kernel.

Since the two interacting ions have independent gyro-phases, the reaction kernel must be averaged over their relative gyro-phase difference $\Delta\phi = \phi_1 - \phi_2$. The relative speed depends on $\Delta\phi$ as

$$v_{\rm rel}(\Delta\phi) = \Big[v_1^2 + v_2^2 - 2v_1v_2\Big(\xi_1\xi_2 + \sqrt{1-\xi_1^2}\sqrt{1-\xi_2^2}\cos\Delta\phi\Big)\Big]^{1/2} \qquad (7)$$

The gyro-phase averaged fusion kernel is therefore defined as

$$\overline{\sigma v}_{12} = \frac{1}{2\pi}\int_0^{2\pi} \sigma(v_{\rm rel}(\Delta\phi))\, v_{\rm rel}(\Delta\phi)\, d(\Delta\phi), \qquad (8)$$

which represents the statistical average over independent gyro-phase angles of the two particles.

In practice, Eq. (8) is evaluated numerically using N_ϕ discrete quadrature points. The pitch integral over ξ is performed using Gauss–Legendre quadrature,

$$\int_{-1}^{1} g(\xi)\, d\xi \approx \sum_{i=1}^{N_\xi} w_i\, g(\xi_i), \qquad (9)$$

where ξ_i and w_i are the Gauss–Legendre nodes and weights, respectively. The energy integrals are computed through discrete summation over the binned distribution. The maximum integration energy is set to $E_{\rm max} = 30\,T_i$ to capture the high-energy tail while avoiding negligible contributions from exponentially small populations.

To validate the implementation, we performed a benchmark using an isotropic Maxwellian distribution of deuterium ions with ion temperature T_i (keV). The computed Maxwellian–Maxwellian reactivity, $\langle\sigma v\rangle_{\rm num}$, was compared against the Bosch–Hale parameterization, $\langle\sigma v\rangle_{\rm BH}$, for the D–D reaction [4]. The relative deviation is defined as

$$\epsilon(T_i)\ [\%] = 100 \times \frac{|\langle\sigma v\rangle_{\rm num}(T_i) - \langle\sigma v\rangle_{\rm BH}(T_i)|}{\langle\sigma v\rangle_{\rm BH}(T_i)}. \qquad (10)$$

For the numerical integration, the energy axis was discretized with $N_E = 32$, 64, and 128 bins. We used $N_\xi = 16$ Gauss–Legendre points for ξ and $N_\phi = 64$ points for the gyro-phase averaging in Eq. (9). Figure 4 shows that increasing N_E reduces the numerical error but increases the elapsed time, indicating a clear accuracy–cost trade-off.

Although $N_E = 128$ can reduce the discretization error to a level comparable to (or below) the intrinsic $\sim 2\%$ uncertainty of the Bosch–Hale parameterization, such resolution is computationally expensive and difficult to employ in full-scale time-dependent simulations. Therefore, we adopt $N_E = 32$ in practical simulations, accepting an error level of approximately $\sim 5\%$ in exchange for substantially improved computational efficiency.

It should be emphasized that the Maxwellian–Maxwellian comparison above serves only to verify the numerical correctness of the fusion integral. In actual simulations, the fusion rate is evaluated from the distribution diagnostics obtained during runtime. The diagnostic constructs a fixed (E, ξ) grid over the selected time interval, and the distribution function is accumulated on this predefined grid.

Because the diagnostic grid remains fixed, the gyro-phase averaged fusion kernel $\overline{\sigma v}_{12}(E_i, \xi_j, E_k, \xi_l)$ can be precomputed and stored for all combinations of grid points. The fusion reaction rate is then obtained through weighted summation over the diagnostic distribution values only, without repeated evaluation of the cross section or gyro-phase integration. This approach substantially reduces computational cost while preserving full consistency with arbitrary, non-Maxwellian distributions.

5. Implementation of the Goosing Scheme in Magnetic Mirror Configuration

In long-time collisional simulations, the characteristic collisional time scale can be significantly longer than the particle orbit time scale. This scale separation leads to excessive computational cost when resolving collisional relaxation processes directly. To address this issue, an acceleration

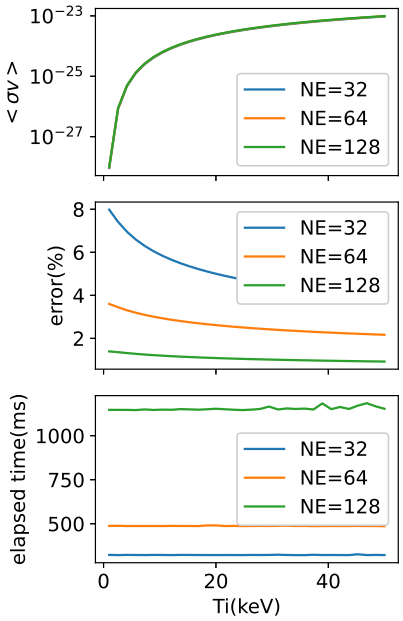

Figure 4: Benchmark of Maxwellian–Maxwellian reactivity for D–D fusion with different energy-bin resolutions. (Top) computed $\langle \sigma v \rangle$; (Middle) relative error with respect to the Bosch–Hale form; (Bottom) elapsed time per evaluation. Cases shown: $N_E = 32$, 64, and 128. Here $N_\xi = 16$ (Gauss–Legendre) and $N_\phi = 64$ for gyro-phase averaging.

technique known as *Goosing* was originally introduced in tokamak simulations [5], where collisional effects are artificially enhanced while preserving the underlying orbit dynamics.

In the present work, the Goosing scheme is implemented for the first time in a magnetic mirror configuration. Although originally developed for toroidal systems, the fundamental concept of separating fast orbit motion from slow collisional relaxation remains applicable to linear mirror devices. However, due to the distinct geometry and particle bounce dynamics in mirror plasmas, a modified event-driven implementation is required.

5.1 Event-Based Formulation Using $z = 0$ Crossing

In a mirror configuration, particle motion along the field line is characterized by periodic bounce trajectories. We define the midplane ($z = 0$) crossing as a natural event marker to segment the orbit into bounce intervals.

Let $z(t)$ denote the particle axial position. A crossing event is detected when the sign of z changes across zero, with a small deadband parameter ε introduced to avoid spurious detections due to numerical noise,

$$\mathrm{sign}_z(z) = \begin{cases} +1 & (z > \varepsilon), \\ -1 & (z < -\varepsilon), \\ 0 & (|z| \le \varepsilon). \end{cases} \tag{11}$$

A crossing is registered when the sign changes between two successive time steps. This event-driven structure divides particle motion into individual bounce segments.

5.2 Segment-Based Accumulation

During each bounce segment, collisional indicators are accumulated. Let the accumulated quantities within a segment be denoted by

$$g_1 = \frac{\Delta V}{V}, \quad g_2 = \Delta\zeta, \quad g_3 = \Delta\zeta_{\mathrm{diff}}, \tag{12}$$

where $\Delta V/V$ represents the relative change in particle speed ($V = |\mathbf{v}|$), $\Delta\zeta$ denotes the mean pitch-angle variation, and $\Delta\zeta_{\mathrm{diff}}$ the pitch-angle fluctuation measure. These quantities characterize the effective collisional evolution during one bounce interval.

Accumulation begins only after the first detected crossing, ensuring that partial initial segments do not bias the evaluation.

5.3 Acceleration Factor Update

At each $z = 0$ crossing event, the acceleration factor is updated based on the accumulated segment quantities. Let

$$g_{\max} = \max(g_1, g_2, g_3),$$

denote the largest normalized collisional modification during a single bounce segment.

In the present implementation, the acceleration factor is updated using a continuous rescaling rule. If G_{ref} denotes the acceleration factor used during the previous bounce segment, the updated factor for the next segment is computed as

$$G_{\mathrm{new}} = \frac{G_{\mathrm{ref}}}{g_{\max}} G_{\mathrm{tol}}, \tag{13}$$

where G_{tol} is a prescribed tolerance parameter that controls the acceptable level of collisional variation per accelerated segment.

When $g_{\max}$ is small, the acceleration factor increases, enhancing computational efficiency. If the collisional modification becomes large, the acceleration factor is automatically reduced, thereby maintaining numerical stability. If $g_{\max} = 0$, the acceleration factor is set to unity. After each update, the segment accumulators are reset, and a new bounce segment begins.

This event-driven formulation ensures that:

- accumulation occurs continuously during orbit integration,
- acceleration updates occur only at physically meaningful bounce boundaries,
- the fast orbit dynamics remain unchanged,
- only the effective collisional relaxation rate is modified.

6. Planned Application to Mirror Devices and Demonstration Outputs

As a demonstration case, counter-injected neutral beams were applied to the previously described mirror equilibrium. A 20 keV deuterium beam with injected power of 1.5 MW and a 20 keV tritium beam with injected power of 1.2 MW were launched from opposite ends of the mirror device toward the central region. The beam inlet width and height were both set to 0.1 m. The background plasma was assumed to have a central density of 2×10^{19} m^{-3} and a deuterium ion temperature of 1 keV. No thermal tritium component was included. Due to the relatively large test device size and the increased plasma density, beam attenuation was

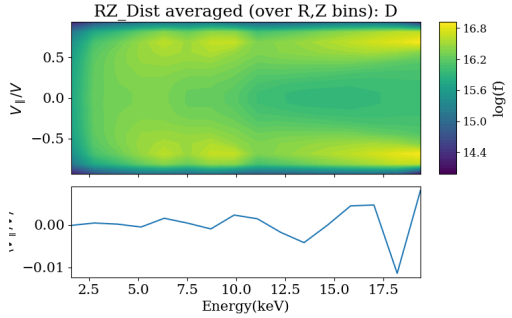

Figure 5: Velocity-space distribution of fast ions generated by a 20 keV, 1.2 MW deuterium beam injection. Top: RZ-averaged distribution $f(v_\parallel/v, E)$ shown in logarithmic scale. Bottom: Energy-dependent pitch parameter $\langle v_\parallel/v \rangle$. The anisotropic structure reflects beam injection geometry and mirror confinement effects.

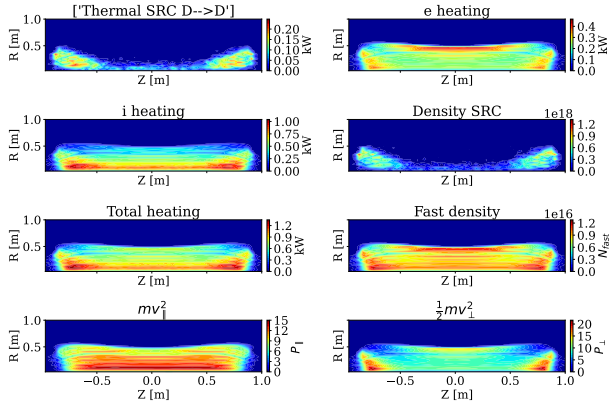

Figure 6: Spatial profiles resulting from 20 keV, 1.2 MW deuterium beam injection with beam width/height of 0.1 m in the mirror equilibrium. From top to bottom and left to right: (a) Thermal source from beam ionization, (b) Electron heating power density, (c) Ion heating power density, (d) Density source rate, (e) Total heating power density, (f) Fast-ion density, (g) Parallel energy density $mv_\parallel^2$, (h) Perpendicular energy density $\frac{1}{2}mv_\perp^2$,

enhanced, resulting in only about 10% shine-through power. This indicates efficient beam deposition within the plasma volume. A total of 6×10^5 test particles were injected over a 50 ms simulation period. Diagnostics were performed over a 5 ms interval from $t = 45$ ms to $t = 50$ ms, during which the fast-ion population reached a quasi-steady state. For the Goosing scheme, the tolerance parameter was set to $G_{\text{tol}} = 0.01$.

Figure 5 shows the velocity-space distribution of fast ions. The pronounced anisotropy reflects directed beam injection from both ends and subsequent pitch-angle scattering under mirror confinement. In the central region where the two beams overlap, collisional redistribution gradually modifies the pitch distribution, leading to partial isotropization.

Figure 6 presents spatial profiles characterizing fast-ion evolution. The top-left panel shows the thermal source, representing the accumulated energy transferred from fast ions to the background plasma through collisional slowing-down, i.e., the total energy of fully thermalized ions. The second-row right panel shows the density source, corresponding to the accumulated weight of thermalized ions, which acts as a particle source to the thermal plasma.

The electron and ion heating power densities illustrate the spatial distribution of collisional energy transfer from fast ions to background species. The total heating profile

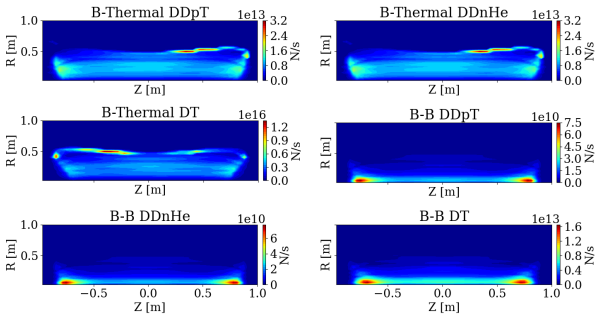

Figure 7: Spatial distributions of fusion reaction rates (s^{-1}) evaluated over $t = 45$–50 ms for counter-injected 20 keV D (1.5 MW) and T (1.2 MW) beams. From top to bottom and left to right: beam–thermal $D+D \rightarrow p+T$, beam–thermal $D + D \rightarrow n + {}^3\text{He}$, beam–thermal $D + T$, beam–beam $D + D \rightarrow p + T$, beam–beam $D + D \rightarrow n + {}^3\text{He}$, and beam–beam $D + T$ reactions. The color scale differs for each panel.

combines these contributions and reflects the overall beam power deposition pattern. The fast-ion density exhibits strong localization along the beam trajectories and near mirror reflection regions, where particles accumulate due to magnetic trapping. Finally, the parallel and perpendicular energy densities ($mv_\parallel^2$ and $\frac{1}{2}mv_\perp^2$) demonstrate anisotropic energy partitioning and mirror-induced pitch-angle redistribution.

Figure 7 shows the spatial distributions of fusion reaction rates. Beam–thermal D–D reactions are concentrated in regions of high fast-ion density, while the beam–thermal D–T channel is localized along the regions where the injected T-beam overlaps with the background deuterium plasma. Beam–beam reactions are enhanced near mirror reflection regions where fast ions accumulate. Among all channels, the beam–beam D–T reaction yields the largest rate, reflecting both the overlap of counter-streaming fast ions and the larger D–T fusion cross section at 20 keV beam energies.

7. Summary

NuBDeC has been successfully extended from tokamak to mirror configuration. A mirror-compatible beam injection routine, a distribution-based beam–beam fusion rate module, and an adaptive Goosing acceleration scheme have been implemented and validated. Benchmarking against Maxwellian reactivity confirms the correctness of the fusion rate calculation, and performance analysis clarifies the trade-off between numerical accuracy and computational cost. These extensions establish a unified computational framework for predictive modeling of beam-driven mirror plasmas.

The present implementation does not yet include charge-exchange collisions of fast ions or heating effects from fusion reaction products. In future work, a detailed charge-exchange collision model will be incorporated to more accurately evaluate fast-ion confinement, neutral losses, and beam attenuation in mirror geometry. In addition, fusion-product heating will be implemented to assess its contribution to the overall plasma energy balance in beam-driven mirror systems.

Furthermore, systematic benchmarking against other established neutral-beam and fast-ion simulation codes will be performed to validate the extended framework under various plasma conditions. A comprehensive optimization study

of the Goosing acceleration parameters is also planned to identify operating regimes in which collisional acceleration is maximized while preserving essential physical invariants. These efforts will ensure numerical robustness and cross-code consistency without compromising physical fidelity.

References

[1] A. V. Anikeev, P. A. Bagryansky, A. D. Beklemishev, A. A. Ivanov, E. Yu. Kolesnikov, M. S. Korzhavina, O. A. Korobeinikova, A. A. Lizunov, V. V. Maximov, S. V. Murakhtin, E. I. Pinzhenin, V. V. Prikhodko, E. I. Soldatkina, A. L. Solomakhin, Yu. A. Tsidulko, D. V. Yakovlev, and D. V. Yurov. Progress in mirror-based fusion neutron source development. *Materials*, 8(12):8452–8459, 2015.

[2] T. Simonen. The status of research regarding magnetic mirrors as a fusion neutron source or power. Technical report, Office of Scientific and Technical Information (OSTI), 2008. Historical context of mirror systems and neutron source concepts.

[3] T. Rhee, K. Shinohara, H.-S. Kim, J. M. Kwon, Y. M. Jeon, J. Kim, S.-H. Hahn, J. G. Kwak, S. J. Wang, B. H. Park, and B. Na. Development of neutral beam deposition code for beam ion dynamics. *Physics of Plasmas*, 26:112504, 2019.

[4] H.-S. Bosch and G. M. Hale. Improved formulas for fusion cross-sections and thermal reactivities. *Nuclear Fusion*, 32(4):611–631, 1992.

[5] R. J. Goldston, D. C. McCune, H. H. Towner, S. L. Davis, R. J. Hawryluk, and G. L. Schmidt. New techniques for accelerating collisional relaxation in plasma simulation. *Journal of Computational Physics*, 43:61–78, 1981.

[6] J. Egedal, D. Endrizzi, C.B. Forest, and T.K. Fowler. Fusion by beam ions in a low collisionality, high mirror ratio magnetic mirror. *Nuclear Fusion*, 62(12):126053, nov 2022.

Acknowledgments

This work was supported by KOREA HYDRO & NUCLEAR POWER CO., LTD (No. 2024-Tech-15). Tongnyeol Rhee was supported by the R&D Program of the Korea Institute of Fusion Energy (KFE), which is funded by the Ministry of Science and ICT of the Republic of Korea (KFE-EN254).